THE JOURNAL OF PHYSICAL CHEMISTRY LETTERS
A JOURNAL OF THE AMERICAN CHEMICAL SOCIETY

pubs.acs.org/JPCL
Letter

Electronic Structures of Iron in Oxide Glasses via 1s3p Resonant Inelastic X-ray Scattering

Yong-Hyun Kim, Jungho Kim, Jung-Fu Lin, and Sung Keun Lee*

Cite This: *J. Phys. Chem. Lett.* 2025, 16, 2627−2635
Read Online

ABSTRACT: Electronic structures of iron in glasses are essential for unraveling the effect of transition metals on amorphous networks and controlling the electro-optical and transport properties of advanced glasses and amorphous energy-storing materials. The electronic configurations around iron in glasses, however, remain not well understood due to the structural disorders arising from multiple iron species with distinct valence, coordination, and spin states. Here, the first 1s3p resonant inelastic X-ray scattering (RIXS) for oxide glasses identifies hidden electronic configurations for Fe^{2+} and Fe^{3+} in amorphous networks. The results allow us to quantify the composition-induced evolution of oxygen ligand−field interactions of high-spin Fe 3d states with varying valence and coordination environments in complex glasses. The distinct electronic structures account for the electronic origins of iron-induced changes in the glass properties. The results offer prospects for a simultaneous probing of valence, coordination, and spin states of transition metals in diverse multicomponent oxide glasses and functional amorphous solids via 1s3p RIXS.

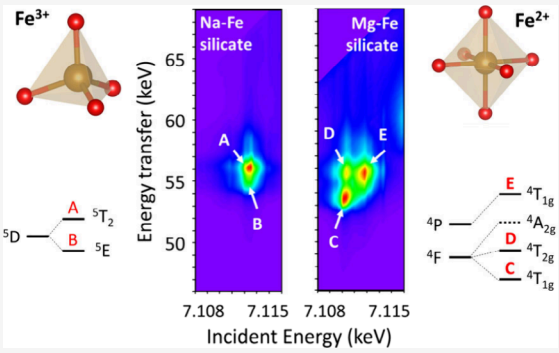

Electronic structures of transition metals in crystalline and amorphous oxides provide the microscopic origins of their distinct chemical, electrical, transport, and magnetic properties. Tuning the electronic configurations of 3d transition metals is crucial for the development of catalysts, batteries, magnetic materials, and light-emitting diodes.[1−3] Particularly, amorphous oxides offer the unique platform to develop the transparent semiconductors and energy-storing materials, as they can store a vast amount of transition metals.[4−7] Iron-bearing silicate glass, as one of the transition-metal-bearing amorphous solids, is a key industrial glass for nuclear waste immobilization and slags.[8−11] The detailed valence, coordination, and electronic spin states of iron in silicate melts and glasses control the elastic-wave velocity and viscosity of magmas in planetary surfaces and interiors.[12−18] Despite the significance, direct probing of the 3d electronic structures of iron and other transition metals in amorphous solids remains a challenge in physical chemistry.

Ferrous (Fe^{2+}) and ferric (Fe^{3+}) irons can coexist in silicate glasses. Their distinct structural roles in the amorphous network, including network-forming (Fe^{3+}, similar to $^{IV}Al^{3+}$) and network-modifying (Fe^{2+}, similar to $^{VI}Mg^{2+}$), have been suggested (see Section S1 for further details).[16,19,20] Other structural environments for both ferric (e.g., $^{V}Fe^{3+}$ or $^{VI}Fe^{3+}$) and ferrous (e.g., $^{IV}Fe^{2+}$ or $^{V}Fe^{2+}$) iron have also been reported for iron-bearing glasses (refs 20−22 and references therein; see Section S2 for earlier efforts). Among useful electronic probes of iron, Mössbauer spectroscopy quantifies the $Fe^{3+}/\Sigma Fe$ and coordination number (CN) of iron in glasses via isomer shifts (IS) and quadrupole splitting (QS) of ^{57}Fe (e.g., refs 23−31). Pioneering efforts with Fe *K*-edge X-ray absorption near-edge structure (XANES) have probed the Fe 3d states in iron-bearing silicates, establishing protocols for the evaluation of $Fe^{3+}/\Sigma Fe$ and CN in silicate glasses from Fe *K* pre-edge features.[20,22,32−37] Electronic spin configurations of iron (i.e., high- or low-spin) have been explored via Fe $K\beta_{1,3}$ X-ray emission spectroscopy (XES), based on the spectral intensity of the satellite features ($K\beta'$).[38−40] Despite the progress, structural disorders (e.g., Fe−O bond distances distribution and coexistence of diverse iron species with multiple valence, coordination, and spin states) in glasses results in gradual variations in spectroscopic parameters, such as IS and QS. Together with the 1s core-hole lifetime broadening (∼1 eV for Fe) in XANES,[41,42] identification of the multiple electron configurations, redox, spin state, and Fe coordination environments in iron-bearing glasses remains challenging.

1s3p resonant inelastic X-ray scattering (RIXS, a.k.a. resonant X-ray emission spectroscopy, RXES; see Section S3 for details on terminology) involves a two-photon process: excitation of 1s electrons into 3d states (or 4p states) and

Received: December 13, 2024
Revised: February 17, 2025
Accepted: February 21, 2025

https://doi.org/10.1021/acs.jpclett.4c03568
J. Phys. Chem. Lett. 2025, 16, 2627−2635

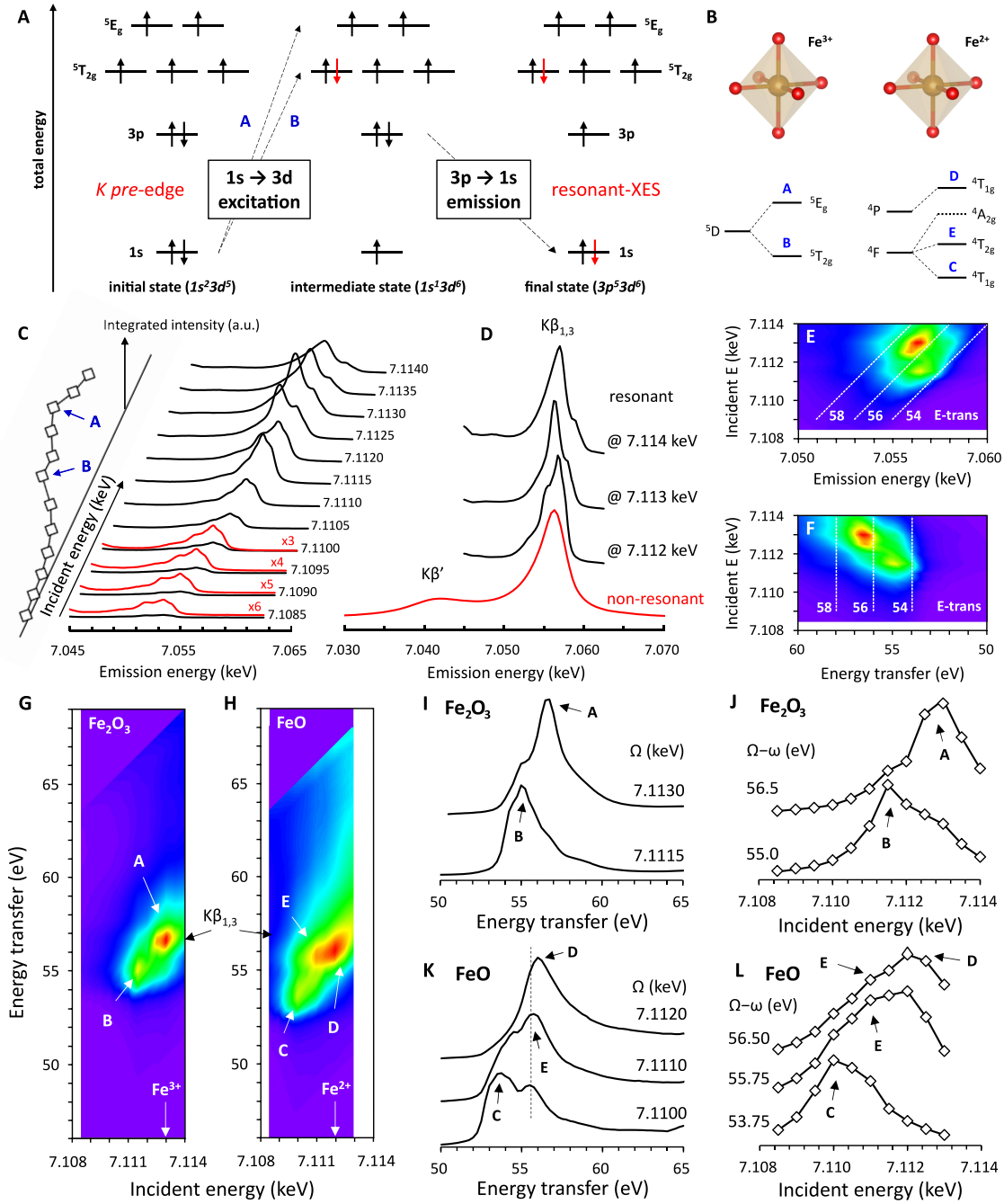

Figure 1. (A) Schematic 1s3p RIXS process for hematite (Fe_2O_3) with $^{VI}Fe^{3+}$. (B) 3d state electronic configurations for crystalline $^{VI}Fe^{2,3+}$. (C) 1s3p RIXS spectra for Fe_2O_3 at ~7.1085−7.1140 keV. (D) 1s3p RIXS spectra and the $K\beta_{1,3}$ XES spectrum for Fe_2O_3. 2D RIXS spectra with (E) emission energy and (F) energy transfer axes. Dashed lines show the constant energy transfer lines of 54, 56, and 58 eV. 2D RIXS spectra for (G) Fe_2O_3 and (H) FeO. (I) Vertical and (J) horizontal RIXS slices for Fe_2O_3 (see Section S5 for further details). (K) Vertical and (L) horizontal RIXS slices for FeO.

probing of the X-ray emission by the transition of 3p electrons into 1s states.[41,43] 1s3p RIXS spectra simultaneously provides the electronic information relevant to the *K*-edge XANES (incident axis) and $K\beta_{1,3}$ XES (emission axis), probing the 3d states of iron and other TMs.[43−56] This resolves the electronic configurations often obscured or overlapped in conventional one-dimensional X-ray spectroscopies. The spectral width for RIXS are further reduced by suppressing core-hole lifetime broadening.[41,57] RIXS has provided high-resolution electronic structures of TM in crystalline electrocatalysts and metal complexes;[41−44,46−48,50,51,54] however, its application to glasses has not been fully demonstrated. High-resolution RIXS of glasses could resolve overlapping electronic configurations from multiple iron species with distinct valence, coordination, and spin.

In the current study, we report the Fe 1s3p RIXS of Fe^{2+}-rich Mg−Fe $[(MgO)_X{\cdot}(FeO)_{1-X}{\cdot}(SiO_2)$ with X = 0.6, 0.8 (MF64 and MF82)] and Fe^{3+}-rich Na−Fe silicate glasses $[(Na_2O)_Y{\cdot}(Fe_2O_3)_{1-Y}{\cdot}2(SiO_2)$ with Y = 0.5, 0.8 (NF55 and NF82)] (see Section S4 and refs 16 and 19 for details on sample synthesis). The Fe 1s3p RIXS measurements were performed with the medium-energy-resolution inelastic X-ray

https://doi.org/10.1021/acs.jpclett.4c03568
J. Phys. Chem. Lett. 2025, 16, 2627−2635

scattering spectrometer at the 30-ID beamline of the Advanced Photon Source (Section S4).[58,59] The spectra were collected by scanning the Fe $K\beta$ emission with varying incident X-ray energies at the Fe 1s → 3d pre-edge in the iron-bearing glasses. The $Fe^{3+}/\Sigma Fe$ values for MF- and NF-glasses were estimated to be ∼0.89 and ∼0.26, respectively (see refs 16 and 19 and references therein). This allows us to explore the interplay between iron valence state with electronic and spin configurations and to uncover the details of 3d electronic configurations of iron in disordered silicate networks, which had remained challenging. We identify the effect of ligand−fields of FeO_X coordination polyhedra on the electron configurations of iron in model crystalline iron oxides and those for complex glasses, offering prospects for exploration of electronic structures of TM-bearing amorphous solids.

■ PROBING OF 3D ORBITALS BY 1S3P RIXS: EXAMPLES WITH MODEL CRYSTALLINE IRON OXIDES

Electronic Transitions Involving 1s3p RIXS of Iron in Metal-Bearing Oxides. As RIXS is an emerging X-ray technique for transition metals in glasses, we briefly describe the utility of 1s3p RIXS with model crystalline compounds (see Sections S5 and S6 for theoretical backgrounds and earlier RIXS efforts on crystalline oxides),[41,42,52,59,60] which are essential to account for spectral features for noncrystalline analogues. The 1s3p RIXS of 3d TM involves the *resonant* excitation of 1s electrons into the unoccupied 3d/4p states and the collection of the $K\beta_{1,3}$ X-ray emissions from the transition of 3p electrons to 1s states [Figure 1(A)].[42,52] The 1s3p RIXS leaves 1s and 3p electron core-holes in the intermediate and final states, respectively. Spectral widths of 1s3p RIXS features are controlled by the core-hole lifetime broadening, where such effects along the incident energy (Ω) or energy transfer axes [($\Omega - w$), where w is emission energy] arise from core-holes in the intermediate or final states.[48] The lifetime of the 3p core-hole is longer than that of the 1s core-hole, reducing the spectral width along the energy transfer axis. This improves spectral resolution, resolving rich electronic configurations of TM,[42,61] which may not be accessed by XANES. The 1s3p RIXS directly probes metal 3d states [Figure 1(B)] and therefore is sensitive to the valence, coordination, and spin states of transition metals (see Section S7 for details on spin states).

Fe 1s3p RIXS of Model Crystalline Compounds. Figure 1(C) shows the 1s3p RIXS spectra for hematite (Fe_2O_3) with varying incident energies from ∼7.1085 to ∼7.1140 keV at the Fe K pre-edge (hereafter, we omitted "pre-edge" for simplicity). RIXS features for iron oxides arise from the $L-S$ coupling of the 3d states for high-spin $^{VI}Fe^{2,3+}$ [Figure 1(B); see Section S7 for effect of spin states on RIXS spectra].[62,63] The Fe^{2+} ($3d^6$) and Fe^{3+} ($3d^5$) exhibit ground state electronic configurations of ^5D and ^6S, respectively, based on the term symbols in the Russell−Saunders coupling scheme (Section S8). The RIXS process results in ^4F or ^4P configurations for Fe^{2+} ($3d^7$) and ^5D for Fe^{3+} ($3d^6$). For Fe^{3+}, O_h symmetry-induced crystal-fields further split ^5D into $^5T_{2g}$ and ^5E_g [Figure 1(B)].[62] Experimental RIXS results resolve these configurations of $^{VI}Fe^{2,3+}$ in these oxides; the spectrum of Fe_2O_3 [Figures 1(C)−1(G)] reveals two major RIXS features at the (Ω, $\Omega - w$) of (∼7.1130 keV, ∼57 eV; peak A) and (∼7.1115 keV, ∼55.5 eV; peak B), which correspond to the electronic transitions of 1s electrons into the ^5E_g and $^5T_{2g}$ states.[64] The observed features correspond to the crystal-field splitting energy of ∼1.4 eV.[42] Current spectral features are consistent with the earlier pioneering RIXS spectra for Fe_2O_3, which have demonstrated the effect of valence states, coordination environments, and spin states on the splitting of RIXS patterns for crystalline oxides.[42,43,47,57,61,64]

The RIXS features shift with increasing incident energy [Figures 1(C) and 1(E)]; such features have constant energy transfers, which are characteristic to electronic excitations into the 3d states.[57] This makes the energy transfer (i.e., $\Omega - w$) axis suitable for the analysis of *pre-edge* 1s3p RIXS spectra [Figure 1(F)]. Note that the RIXS features from the excitation into the 4p states (i.e., main-edge) exhibits constant *emission* energies, similar to nonresonant XES.[42,57] Figure 1(D) shows the 1s3p RIXS and $K\beta_{1,3}$ XES spectra of Fe_2O_3; whereas the $K\beta_{1,3}$ XES exhibits a single broad peak, the 1s3p RIXS spectrum reveals multiple fine features. The enhanced spectral resolution stems from the difference in the number of 3d electrons in the final states of RIXS and XES (i.e., $3p^53d^6$ and $3p^53d^5$, respectively),[61] as the former provides the access to multiple electronic configurations.

Fe 1s3p RIXS spectrum for FeO-wüstite [Fe-endmember of (Mg,Fe)O] highlights the electronic configurations of $^{VI}Fe^{2+}$ [Figure 1(H)]. The O_h symmetry-induced crystal-field splits ^4F into $^4T_{1g}$, $^4T_{2g}$, and $^4A_{2g}$ and ^4P into $^4T_{1g}$ [Figure 1(B)].[62] The spectrum of FeO reveals two major RIXS features at the (Ω, $\Omega - w$) of (∼7.110 keV, ∼54 eV; peak C), (∼7.112 keV, ∼56 eV; peak D), with a minor feature at (∼7.111 keV, ∼56 eV; peak E), which correspond to the $^4T_{1g}$ (^4F), $^4T_{1g}$ (^4P), and $^4T_{2g}$ (^4F) states of $^{VI}Fe^{2+}$, respectively. The $^4A_{2g}$ state, which involves the excitations of two electrons, is forbidden in the RIXS.[62,65] Note that our 1s3p RIXS spectrum for FeO is overall consistent with that for $Mg_{0.95}Fe_{0.05}O$ from earlier studies.[42,48]

Horizontal and vertical projections of 2D RIXS spectra allow for a detailed examination of excitations at the specific energy transfer and incident energy, respectively (see Sections S4 and S5 with Figures S1 and S2 for additional details). Figures 1(I) and 1(J) show the RIXS slices for Fe_2O_3 with varying incident energies and energy transfers, respectively; peak B and peak A are selectively excited at the Ω of ∼7.1115 keV and ∼7.1130 keV and ($\Omega - w$) of ∼55.0 eV and ∼56.5 eV, respectively. Figure 1(K) shows the RIXS slices for FeO at the energy transfer axis; peaks C and E are observed at ∼7.110 keV, and an intensity of peak E further increases at ∼7.111 keV. At ∼7.112 keV, peak D [i.e., $^4T_{1g}$ (^4P)] appears at the energy transfer of ∼56 eV. Note that peak E [i.e., $^4T_{2g}$ (^4F)] is often difficult to resolve in the XANES because of its overlap with $^4T_{1g}$ features.[20,32,36,66] In contrast, the 1s3p RIXS resolves those features for $^{VI}Fe^{2+}$ by introducing an additional energy transfer dimension. The RIXS slices along the incident energy axis [Figure 1(L)] also resolve those features as the peak intensities evolve with varying intensities ($\Omega - w$). The Ω values of the main RIXS features for $^{VI}Fe^{2+}$ and $^{VI}Fe^{3+}$ are ∼7.112 and ∼7.113 keV, respectively. The difference results from an increase in the metal valence states, consistent with those of ∼1.4 eV in the *pre-edge* centroid positions for $Fe^{2,3+}$ from earlier XANES studies.[20,32,36] The results with the model compounds confirm that 1s3p RIXS is an effective probe of the 3d electronic configurations.

https://doi.org/10.1021/acs.jpclett.4c03568
J. Phys. Chem. Lett. 2025, 16, 2627−2635

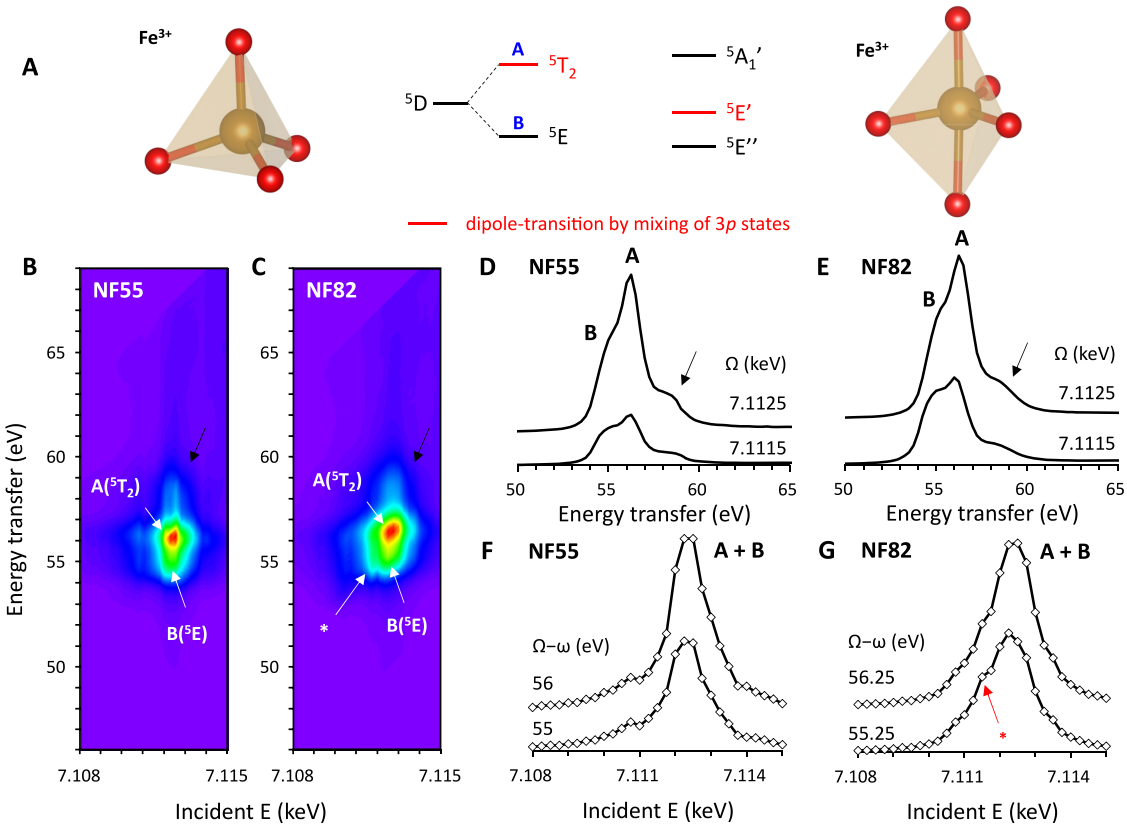

Figure 2. (A) Schematic illustration of the 3d-orbital energy distributions for $^{IV}Fe^{3+}$ and $^{V}Fe^{3+}$. 1s3p RIXS 2D plot for (B) NF55 and (C) NF82 glasses. (D) Vertical and (E) horizontal slices of the 1s3p RIXS spectra for iron-bearing sodium silicate glass, NF55. (F) Vertical and (G) horizontal slices of the 1s3p RIXS spectra for iron-bearing sodium silicate glass, NF82.

■ ELECTRONIC CONFIGURATIONS OF FERRIC IRON IN NA−FE SILICATE GLASS VIA 1S3P RIXS

The RIXS results from the crystalline oxides with well-defined structures (e.g., valence states, coordination environments, and spin configurations) provide a reference to explore the electronic configurations of iron-bearing silicate glasses with multiple iron species. Fe 1s3p RIXS reveals the electronic configurations of Fe^{3+} in Na−Fe silicate glasses, NF55 and NF82, with $Fe^{3+}/\Sigma Fe$ of ∼0.89 ± 0.04 (ref 19) (Figure 2). The RIXS planes of the NF-glass reveal the major feature at (∼7.1125 keV, ∼56 eV; peak A) with a minor feature at (∼7.1125 keV, ∼55 eV; peak B) [Figures 2(B) and 2(C)]; spectral patterns are clearly different from the Fe_2O_3 crystal (Figure 1), indicating the distinct structural environments of Fe^{3+} in the silicate glasses. Vertical slices of the RIXS spectra [Figures 2(D) and 2(E)] reveal prominent features at ∼55 eV (peak B) and ∼56 eV (peak A), with a minor feature at ∼58.5 eV. The spectral intensities of these features increase at ∼7.1125 keV. The horizontal slices of the RIXS spectra [Figures 2(F) and 2(G)] show an intense feature at ∼7.1125 keV, with a shoulder at ∼7.1115 keV. The 1s3p RIXS slices of the NF82 glass show an increase in the spectral intensity at ∼7.1115 keV [red arrow with an asterisk in Figure 2(G)], as observed in the 2D RIXS plot [Figure 2(C)].

The *multiplet* features in the RIXS spectra of the NF glass originate from the Fe−O ligand−field-induced splitting of the ^5D state for Fe^{3+}. Particularly, the T_d-symmetry splits the ^5D state into $^5T_2$ and ^5E [Figure 2(A)], which accounts for the peaks A and B in the RIXS spectra, respectively. The spectral results indicate the $^{IV}Fe^{3+}$ dominance in the NF-silicate glasses,[62,65] as electronic configurations for other coordination environments [e.g., $^{VI}Fe^{3+}$ in Figure 1(B) or $^{V}Fe^{3+}$ in Figure 2(A)] may not explain the main RIXS features. The spectral features are rather similar to the RIXS spectra of $^{IV}Fe^{3+}$ in crystalline oxides (Section S6).[47,57] The A ($^5T_2$) peak further gains intensity by the dipole-allowed electronic transitions into mixed 3d−4p states,[62] accounting for the enhanced spectral intensity of peak A relative to peak B [red marks in Figure 2(A)]. The minor feature at ∼58.5 eV [black arrows in Figures 2(B)−2(E)] corresponds to a final-state 3p−3d electron configuration (i.e., $3p^53d^6$) at the lower energy level, which could arise from electron−electron charge multiplet interactions of the 3p−3d states, as shown by earlier RIXS simulations for $^{IV}Fe^{3+}$.[61] Theoretical studies on the shift in spectral features in glasses due to the changes in local coordination environments remain.

Multiple iron species with distinct valence states and CN coexist in the iron-bearing silicate glasses. The RIXS spectra for NF-glasses also reveal additional minor features below the Ω value of ∼7.111 keV [Figures 2(B)−2(E)]. Based on the lower Ω values for Fe^{2+} ions in crystalline oxides [Figures 1(J) and 1(L)], these could stem from the minor fractions of Fe^{2+} in the NF glass, while weak intensity makes it difficult to identify the CN of Fe^{2+}. Finally, the 2D RIXS plot for NF82 reveals spectral intensities at (∼7.1118 keV, ∼55 eV) [arrows with asterisks in Figures 2(C) and 2(G)]. They could stem from the formation of $^{V}Fe^{3+}$ or the distortion of $^{IV}Fe^{3+}$ in the NF glasses. First, the trigonal bipyramid geometry (D_{3h}) of $^{V}Fe^{3+}$ splits the 3d levels into $^5A_1'$ (d_{z2}), $^5E'$ (d_{xy} and d_{x2-y2}), and $^5E''$ (d_{xz} and d_{yz}). With D_{3h} symmetry, transition to $^5A_1'$ and $^5E''$ is only

https://doi.org/10.1021/acs.jpclett.4c03568
J. Phys. Chem. Lett. 2025, 16, 2627−2635

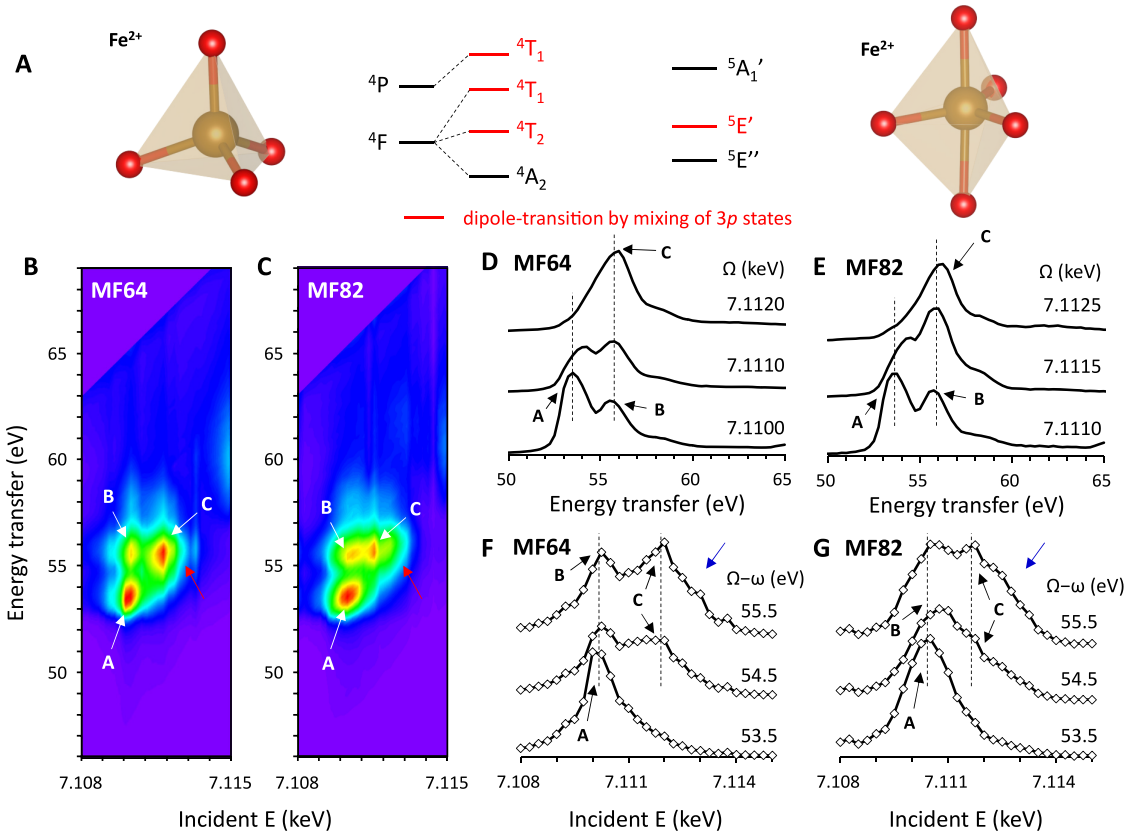

Figure 3. (A) Schematic illustration of the 3d orbital energy distributions for $^{IV}Fe^{2+}$ and $^{V}Fe^{2+}$. 1s3p RIXS 2D plot for (B) MF64 and (C) MF82 glasses. (D) Vertical and (E) horizontal slices of the 1s3p RIXS spectra for iron-bearing magnesium silicate glass, MF64. (F) Vertical and (G) horizontal slices of the 1s3p RIXS spectra for iron-bearing magnesium silicate glass, MF82.

available by the quadrupole transitions, while $^5E'$ enables the mixing of 4p states, allowing both quadrupole- and dipole-allowed transitions.[67,68] The RIXS features for $^{V}Fe^{3+}$ are dominated by the peak from $^5E'$ states, whereas other signals from $^5E''$ and $^5A_1'$ states involving only quadrupole transitions are suppressed in the RIXS spectra. Second, this feature could be due to an increase in the structural distortions in $^{IV}Fe^{3+}$, which breaks the local symmetries and promotes the mixing of the p states.[22] Meanwhile, the horizontal slice of RIXS spectra [a red asterisk in Figure 2(G)] indicates that the spectral feature at ∼7.1115 keV is distinct from ^5E states of $^{IV}Fe^{3+}$ at ∼7.1125 keV. The distortion of $^{IV}Fe^{3+}$ may also increase the spectral widths of the $^5T_2$ and ^5E states, because a gradual variation in the local atomic configurations alters the ligand−field of the FeO_X polyhedra to further shift and/or broaden the spectral features. The current RIXS results without showing clear spectral broadening indicate the formation of $^{V}Fe^{3+}$ in the NF glass, rather than the distortion of the $^{IV}Fe^{3+}$.

■ ELECTRONIC CONFIGURATIONS OF FERROUS IRON IN THE MG−FE SILICATE GLASS VIA 1S3P RIXS

Figure 3 shows the Fe 1s3p RIXS results for Mg−Fe silicate glasses, MF64 and MF82, with the dominant iron redox states of Fe^{2+} (i.e., $Fe^{3+}/\Sigma Fe \approx 0.26$ for MF82 glass; see ref 16 for further details). Figure 3(A) shows 3d electronic configurations for Fe^{2+} in tetrahedral and trigonal bipyramid symmetry. The 2D RIXS spectra of MF-glass are rather complex, overall consisting of three major features at (∼7.1103 keV, ∼53.5 eV; peak A), (∼7.1103 keV, ∼55.5 eV; peak B), and (∼7.1120 keV, ∼55.5 eV; peak C) [Figures 3(B) and 3(C)]. Other minor features are observed at the energy transfer of ∼57−60 eV, which can be attributed to multiplet structures from electron−electron correlations for $^{IV}Fe^{2+}$.[61] The vertical slices of the RIXS spectra [Figures 3(D) and 3(E)] show features at ∼53.5 eV (peak A) and ∼55.5 eV (peaks B and C), similar to $^{VI}Fe^{2+}$ in the crystalline FeO [Figure 1(K)]. However, peak A for MF-glass is much more intense than that for crystalline FeO. The peak A is prominent at the Ω of ∼7.110 keV, while the peaks B and C can be observed at the Ω of ∼7.110−7.112 keV. While peaks A and B cannot be resolved in the incident energy dimension [Figures 3(F) and 3(G)], 2D RIXS spectra fully resolve the features A and B from two distinct final states. We note that these features cannot be fully resolved in the XANES of Fe^{2+}-bearing silicate glasses.[23,25,39,69] At the $(\Omega - w)$ of ∼55.5 eV, the horizontal slices reveal the features at ∼7.112 keV with high-energy tails up to ∼7.113 keV [blue arrows in Figures 3(F) and 3(G), red arrows in Figures 3(B) and 3(C)]. The spectral intensity above ∼7.112 keV increases for the MF64 glass relative to the MF82 glass.

Considering the dominance of $^{VI}Fe^{2+}$ in MF silicate glass,[23,24,30] the peaks A, B, and C can be attributed to the $^4T_{1g}(^4F)$, $^4T_{2g}(^4F)$, and $^4T_{1g}(^4P)$ states [Figure 1(B)]. The positions and intensities of the features for glasses are distinct from those of crystalline $^{VI}Fe^{2+}$; horizontal slices show the peak B at the $(\Omega - w)$ of ∼55.5 eV, while the feature was absent in the FeO crystal. In addition, the peak A for the MF glass is much more intense than that in the FeO crystal. This

https://doi.org/10.1021/acs.jpclett.4c03568
J. Phys. Chem. Lett. 2025, 16, 2627−2635

difference originates partly from the structural distortion around Fe in the MF glass, breaking the octahedral symmetry. The distortion alters the ligand−fields, shifting the energy levels of the 3d states. The distortion of O_h sites further allows the mixing of the 3d−4p states, which induces additional dipole transitions to enhance the spectral intensity.[42] The distortion-induced increase in the spectral intensity of pre-edge has been demonstrated for crystalline oxides.[20,63] While the effect of distortion on spectral intensities of amorphous oxides has not yet been fully established, the rise of the peak A intensity may stem from the mixing of $^4T_{1g}$ states with the p states. Future theoretical calculations on disordered systems with varying iron atomic configurations (e.g., Fe−O lengths and/or bond angles) are necessary to quantify the distortion-induced changes in the electronic configurations.

Alternatively, the increase in the intensity of peak A, with the emergence of peak B, could arise from the presence of other iron coordination environments, $^{IV}Fe^{2+}$ and $^{V}Fe^{2+}$ [Figure 3(A)]. For $^{IV}Fe^{2+}$, three electronic states can be mixed with the p states,[62,63,65] which may give rise to three intense features in the RIXS spectra. However, no strong evidence of such features was observed in the current results. Meanwhile, for $^{V}Fe^{2+}$ within D_{3h} symmetry,[67,68] the RIXS feature is expected to consist of a $^5E'$ state with two weak features from the $^5E''$ and $^5A_1'$ states. As the $^5E'$ state of $^{V}Fe^{2+}$ and the $^4T_{1g}$ state of $^{VI}Fe^{2+}$ can both exhibit spectral features at Ω of ∼7.110 keV,[62,68] $^{V}Fe^{2+}$ could account for the intense peak A in the MF-silicate glasses. Note that the intensity of the pre-edge features from $^{V}Fe^{2+}$ is often larger than $^{VI}Fe^{2+}$ due to their effective mixing with p states.[22,32] Finally, considering the lower Ω range of ∼7.110 keV, the intense peak is not due to Fe^{3+}.

Furthermore, the RIXS spectra reveal high-energy tails above ∼7.112 keV at the $(\Omega - w)$ of ∼55.5 eV [blue arrows in Figures 3(F) and 3(G)]. Considering that RIXS spectra for Fe^{3+} exhibit spectral intensity in the ∼7.112−7.114 keV range, the features could arise from Fe^{3+} in MF-silicate glasses. Our RIXS spectra for MF64 glass show an increase in the intensity around ∼7.112 keV, relative to MF82 glass, indicating an increase in the Fe^{3+} fraction, consistent with an earlier report where an increase in the total iron contents increases the $Fe^{3+}/\Sigma Fe$.[21] Whereas improvements in the energy resolutions and X-ray photon fluxes for RIXS will further better identify minor spectral features and their electronic origins, our current two-dimensional experimental results resolve previously hidden electron configurations of iron-bearing silicate glasses.

1S3P RIXS AS AN ELECTRONIC STRUCTURAL PROBE OF AMORPHOUS SOLIDS AND GLASSES

As described in previous sections, RIXS reduces the spectral width along the energy transfer axis, providing enhanced spectral resolution for 3d configurations of transition metals. Figure 4 shows the projected 1s3p RIXS spectra for the model iron oxides and silicate glasses along the energy transfer axis. The projected spectra resolved multiple spectral features for distinct Fe^{2+} and Fe^{3+} configurations. The projected spectra also resolve the ligand−field-induced splitting of 3d states (e.g., ^5E and $^5T_2$ for NF glasses) and enable estimation of the Fe CN in glasses, which may not be effectively accessed by other conventional probes. Figure 4(B) shows that RIXS features evolve with varying incident X-ray energies. These features resonate at specific incident energies, providing additional spectral resolution by tuning the energy windows. The

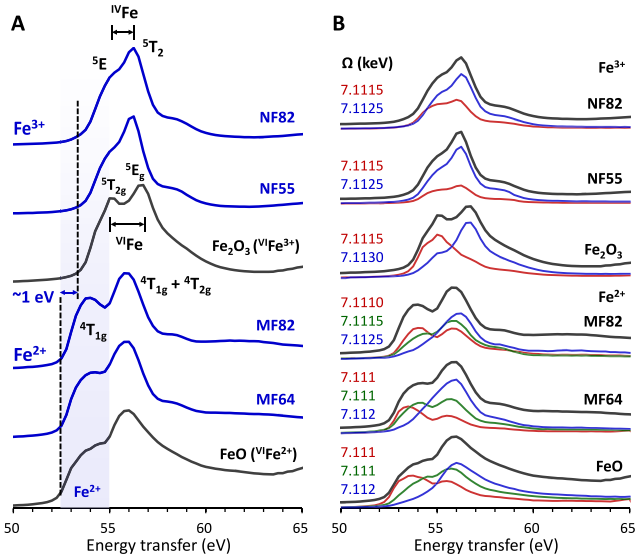

Figure 4. (A) Projection of 1s3p RIXS spectra for model iron oxides and silicate glasses along the energy transfer axis. (B) Projection of 1s3p RIXS spectra (black) with RIXS slices at chosen incident energies (red, blue, and green), as labeled.

projection of RIXS features along the energy transfer axis, together with RIXS slices at selected incident X-ray energies [Figure 4(B)], can be a new and effective probe of the valence, coordination, and spin configurations of amorphous materials.

In this study, the first Fe 1s3p RIXS spectra for silicate glasses reveal the 3d electronic configurations for Fe^{2+} and Fe^{3+} in complex iron-bearing silicate glasses. Despite their structural disorders, RIXS resolves multiple spectral features that originate from the complex electronic bonding environments, thereby revealing the effect of redox states and CN on the electronic structures of iron in glasses. The distinct CN of iron, particularly, $^{IV}Fe^{3+}$ and $^{VI}Fe^{2+}$ are dominant species in the Na−Fe^{3+} and Mg−Fe^{2+} glasses, respectively, generally consistent with their network-forming and network-modifying roles. The RIXS spectra also identify the spectral patterns from minor iron species due to the $^{V}Fe^{3+}$ in Na−Fe^{3+} and $^{V}Fe^{2+}$ in Mg−Fe^{2+} glasses. The distinct electronic structures of those iron species, arising from the interplay of iron redox states, oxygen ligand−fields, and electronic spin configurations, affect the bond strengths of FeO_X polyhedra, which account for the electronic origin of the degree of melt polymerization and viscosity of the silicate melts.[12,13] Furthermore, because charge-carrier mobility of transition metal oxides arises from *partially filled* 3d states, complex ligand effects on the 3d electronic configurations of amorphous networks have direct impact on the electrical conductivity of iron-bearing silicate glasses.[69] Our spectroscopic results will aid in establishing the structural origins of the physical and chemical properties of basaltic (Mg−Fe^{2+} rich) and more oxidized rhyolitic silicate glasses and melts at varying pressure, temperature, melt composition, and/or oxygen fugacity in planetary surfaces and interiors.

Finally, while the RIXS has been used for crystalline TM-oxides, electrocatalysts, and metal complexes,[44,46,47,51,55,56,58,70,71] its application to *amorphous* oxides remained. The current study demonstrates that RIXS, which can integrate electronic information from both X-ray absorption and X-ray emission spectroscopies, is a suitable

https://doi.org/10.1021/acs.jpclett.4c03568
J. Phys. Chem. Lett. 2025, 16, 2627−2635

experimental probe for iron redox, coordination environments, and electronic spin states of iron-bearing amorphous materials. RIXS can fully isolate pre-edge features from the intense background and reduce the core-hole lifetime broadening effects, providing a robust way to estimate the atomic structures of iron-bearing silicate glasses. These first high-resolution electronic structures of iron-bearing glasses offer inspiration to explore the atomic structures and electronic properties of disordered TM-bearing amorphous solids.

■ ASSOCIATED CONTENT

Supporting Information

The Supporting Information is available free of charge at https://pubs.acs.org/doi/10.1021/acs.jpclett.4c03568.

Structural behavior of cations in the oxide glasses; summary of earlier efforts on the redox and coordination of iron in silicate glasses; terminology—resonant inelastic X-ray scattering vs. resonant X-ray emission spectroscopy; additional experimental details; theoretical backgrounds of resonant inelastic X-ray scattering; summary of earlier efforts on the RIXS of crystalline materials; electronic spin configuration of ferrous and ferric iron and resonant inelastic X-ray scattering; term symbols of ferrous and ferric iron (PDF)

■ AUTHOR INFORMATION

Corresponding Author

Sung Keun Lee − *Laboratory of Physics and Chemistry of Earth Materials, School of Earth and Environmental Sciences, Seoul National University, Seoul 08826, Korea; Institute of Applied Physics, Seoul National University, Seoul 08826, Korea;* orcid.org/0000-0002-3149-3421; Email: sungklee@snu.ac.kr; https://g2mat.snu.ac.kr

Authors

Yong-Hyun Kim − *Laboratory of Physics and Chemistry of Earth Materials, School of Earth and Environmental Sciences, Seoul National University, Seoul 08826, Korea;* orcid.org/0000-0002-8579-4131

Jungho Kim − *Advanced Photon Source, Argonne National Laboratory, Argonne, Illinois 60439, United States;* orcid.org/0000-0003-4560-6375

Jung-Fu Lin − *Department of Earth and Planetary Sciences, Jackson School of Geosciences, The University of Texas at Austin, Austin, Texas 78712, United States*

Complete contact information is available at: https://pubs.acs.org/10.1021/acs.jpclett.4c03568

Author Contributions

S.K.L. and J.L. developed the project. S.K.L. acquired funding and supervised the project. J.K. and S.K.L. provided methodology. S.K.L., J.K., and J.L. performed the RIXS experiment in 2011. Y.H.K. analyzed the data. Y.H.K. prepared the original draft. S.K.L. revised the draft. All authors commented on the manuscript.

Notes

The authors declare no competing financial interest.

■ ACKNOWLEDGMENTS

This work was supported by the Research Leader program of the National Research Foundation of Korea (NRF) Grant (NRF-2020R1A3B2079815) to S.K.L. Y.H.K. is supported by the Postdoctoral Fellowship program (NRF RS-2023-00271109). Portions of this work were performed at the MERIX beamline (30-ID), Advanced Photon Source (APS), Argonne National Laboratory (ANL). The APS is a user facility operated for the DOE Office of Science by ANL under Contract DE-AC02-06CH11357. We thank Hyo-Im Kim and Bum Han Lee for glass synthesis. We thank two anonymous reviewers and the editor for constructive comments and inputs, which improve the quality of the manuscript.

■ REFERENCES

(1) Kalyanasundaram, K.; Grätzel, M. Applications of Functionalized Transition Metal Complexes in Photonic and Optoelectronic Devices. *Coord. Chem. Rev.* **1998**, *177* (1), 347−414.

(2) Nazeeruddin, M. K.; Grätzel, M. Transition Metal Complexes for Photovoltaic and Light Emitting Applications. In *Photofunctional Transition Metal Complexes*, Yam, V. W. W., Ed.; Springer Berlin Heidelberg, 2007; pp 113−175.

(3) Nandy, A.; Duan, C.; Taylor, M. G.; Liu, F.; Steeves, A. H.; Kulik, H. J. Computational Discovery of Transition-Metal Complexes: From High-Throughput Screening to Machine Learning. *Chem. Rev.* **2021**, *121* (16), 9927−10000.

(4) Lu, B.; Zhuge, F.; Zhao, Y.; Zeng, Y.-J.; Zhang, L.; Huang, J.; Ye, Z.; Lu, J. Amorphous Oxide Semiconductors: From Fundamental Properties to Practical Applications. *Curr. Opin. Solid State Mater. Sci.* **2023**, *27* (4), 101092.

(5) Murawski, L.; Barczyński, R. J. Dielectric Properties of Transition Metal Oxide Glasses. *J. Non-Cryst. Solids* **1995**, *185* (1), 84−93.

(6) Jiang, Y.; Zhang, D.; Li, Y.; Yuan, T.; Bahlawane, N.; Liang, C.; Sun, W.; Lu, Y.; Yan, M. Amorphous Fe_2O_3 as a High-Capacity, High-Rate and Long-Life Anode Material for Lithium Ion Batteries. *Nano Energy* **2014**, *4*, 23−30.

(7) Duclot, M.; Souquet, J.-L. Glassy Materials for Lithium Batteries: Electrochemical Properties and Devices Performances. *J. Power Sources* **2001**, *97−98*, 610−615.

(8) Shi, C.; Alderman, O. L. G.; Tamalonis, A.; Weber, R.; You, J.; Benmore, C. J. Redox-Structure Dependence of Molten Iron Oxides. *Commun. Mater.* **2020**, *1* (1), 80.

(9) Mancini, A.; Lothenbach, B.; Geng, G.; Grolimund, D.; Sanchez, D. F.; Fakra, S. C.; Dähn, R.; Wehrli, B.; Wieland, E. Iron Speciation in Blast Furnace Slag Cements. *Cem. Concr. Res.* **2021**, *140*, 106287.

(10) Piatak, N. M.; Parsons, M. B.; Seal, R. R. Characteristics and Environmental Aspects of Slag: A Review. *Appl. Geochem.* **2015**, *57*, 236−266.

(11) Magnien, V.; Neuville, D. R.; Cormier, L.; Roux, J.; Hazemann, J. L.; Pinet, O.; Richet, P. Kinetics of Iron Redox Reactions in Silicate Liquids: A High-Temperature X-Ray Absorption and Raman Spectroscopy Study. *J. Nucl. Mater.* **2006**, *352* (1), 190−195.

(12) Mysen, B.; Richet, P. *Silicate Glasses and Melts*; Elsevier, 2019.

(13) Dingwell, D. B.; Virgo, D. The Effect of Oxidation State on the Viscosity of Melts in the System Na_2O-FeO-Fe_2O_3-SiO_2. *Geochim. Cosmochim. Acta* **1987**, *51* (2), 195−205.

(14) Mao, W. L.; Mao, H.-k.; Sturhahn, W.; Zhao, J.; Prakapenka, V. B.; Meng, Y.; Shu, J.; Fei, Y.; Hemley, R. J. Iron-Rich Post-Perovskite and the Origin of Ultralow-Velocity Zones. *Science* **2006**, *312* (5773), 564−565.

(15) Lin, J.-F.; Speziale, S.; Mao, Z.; Marquardt, H. Effects of the Electronic Spin Transitions of Iron in Lower Mantle Minerals: Implications for Deep Mantle Geophysics and Geochemistry. *Rev. Geophys.* **2013**, *51* (2), 244−275.

(16) Kim, H.-I.; Lee, S. K. The Degree of Polymerization and Structural Disorder in (Mg,Fe)SiO_3 Glasses and Melts: Insights from High-Resolution ^{29}Si and ^{17}O Solid-State NMR. *Geochim. Cosmochim. Acta* **2019**, *250*, 268−291.

(17) Caracas, R. The Thermal Equation of State of the Magma Ocean. *Earth Planet. Sci. Lett.* **2024**, *637*, 118724.

(18) Ghosh, D. B.; Karki, B. B. Effects of Valence and Spin of Fe in $MgSiO_3$ Melts: Structural Insights from First-Principles Molecular Dynamics Simulations. *Geochim. Cosmochim. Acta* **2020**, *279*, 107−118.
(19) Kim, H.-I.; Sur, J. C.; Lee, S. K. Effect of Iron Content on the Structure and Disorder of Iron-Bearing Sodium Silicate Glasses: A High-Resolution ^{29}Si and ^{17}O Solid-State NMR Study. *Geochim. Cosmochim. Acta* **2016**, *173*, 160−180.
(20) Wilke, M.; Farges, F.; Partzsch, G. M.; Schmidt, C.; Behrens, H. Speciation of Fe in Silicate Glasses and Melts by in-Situ XANES Spectroscopy. *Am. Mineral.* **2007**, *92* (1), 44−56.
(21) Mysen, B. O. The Structural Behavior of Ferric and Ferrous Iron in Aluminosilicate Glass near Meta-Aluminosilicate Joins. *Geochim. Cosmochim. Acta* **2006**, *70* (9), 2337−2353.
(22) Wilke, M.; Partzsch, G. M.; Bernhardt, R.; Lattard, D. Determination of the Iron Oxidation State in Basaltic Glasses Using XANES at the K-Edge. *Chem. Geol.* **2004**, *213* (1), 71−87.
(23) Nolet, D. A. Optical Absorption and Mössbauer Spectra of Fe, Ti Silicate Glasses. *J. Non-Cryst. Solids* **1980**, *37* (1), 99−110.
(24) Virgo, D.; Mysen, B. O. The Structural State of Iron in Oxidized vs. Reduced Glasses at 1 atm: A ^{57}Fe Mössbauer Study. *Phys. Chem. Miner.* **1985**, *12* (2), 65−76.
(25) Hannoyer, B.; Lenglet, M.; Dürr, J.; Cortes, R. Spectroscopic Evidence of Octahedral Iron (III) in Soda-Lime Silicate Glasses. *J. Non-Cryst. Solids* **1992**, *151* (3), 209−216.
(26) Roskosz, M.; Dauphas, N.; Hu, J.; Hu, M. Y.; Neuville, D. R.; Brown, D.; Bi, W.; Nie, N. X.; Zhao, J.; Alp, E. E. Structural, Redox and Isotopic Behaviors of Iron in Geological Silicate Glasses: A NRIXS Study of Lamb-Mössbauer Factors and Force Constants. *Geochim. Cosmochim. Acta* **2022**, *321*, 184−205.
(27) Solomatova, N. V.; Jackson, J. M.; Sturhahn, W.; Rossman, G. R.; Roskosz, M. Electronic Environments of Ferrous Iron in Rhyolitic and Basaltic Glasses at High Pressure. *J. Geophys. Res.: Solid Earth* **2017**, *122* (8), 6306−6322.
(28) Dyar, M. D. A Review of Mössbauer Data on Inorganic Glasses: The Effects of Composition on Iron Valency and Coordination. *Am. Mineral.* **1985**, *70* (3−4), 304−316.
(29) Rossano, S.; Behrens, H.; Wilke, M. Advanced Analyses of ^{57}Fe Mössbauer Data of Alumino-Silicate Glasses. *Phys. Chem. Miner.* **2008**, *35* (2), 77−93.
(30) Mysen, B. O.; Seifert, F.; Virgo, D. Structure and Redox Equilibria of Iron-Bearing Silicate Melts. *Am. Mineral.* **1980**, *65* (9−10), 867−884.
(31) Ahmadzadeh, M.; Scrimshire, A.; Mottram, L.; Stennett, M. C.; Hyatt, N. C.; Bingham, P. A.; McCloy, J. S. Structure of $NaFeSiO_4$, $NaFeSi_2O_6$, and $NaFeSi_3O_8$ Glasses and Glass-Ceramics. *Am. Mineral.* **2020**, *105* (9), 1375−1384.
(32) Wilke, M.; Farges, F. o.; Petit, P.-E.; Brown, G. E., Jr; Martin, F. o. Oxidation State and Coordination of Fe in Minerals: An Fe *K*-XANES Spectroscopic Study. *Am. Mineral.* **2001**, *86* (5−6), 714−730.
(33) Alderman, O. L. G.; Wilding, M. C.; Tamalonis, A.; Sendelbach, S.; Heald, S. M.; Benmore, C. J.; Johnson, C. E.; Johnson, J. A.; Hah, H. Y.; Weber, J. K. R. Iron *K*-Edge X-Ray Absorption near-Edge Structure Spectroscopy of Aerodynamically Levitated Silicate Melts and Glasses. *Chem. Geol.* **2017**, *453*, 169−185.
(34) Alderman, O. L. G.; Lazareva, L.; Wilding, M. C.; Benmore, C. J.; Heald, S. M.; Johnson, C. E.; Johnson, J. A.; Hah, H. Y.; Sendelbach, S.; Tamalonis, A.; et al. Local Structural Variation with Oxygen Fugacity in Fe_2SiO_{4+X} Fayalitic Iron Silicate Melts. *Geochim. Cosmochim. Acta* **2017**, *203*, 15−36.
(35) Farges, F.; Lefrère, Y.; Rossano, S.; Berthereau, A.; Calas, G.; Brown, G. E. The Effect of Redox State on the Local Structural Environment of Iron in Silicate Glasses: A Combined XAFS Spectroscopy, Molecular Dynamics, and Bond Valence Study. *J. Non-Cryst. Solids* **2004**, *344* (3), 176−188.
(36) Berry, A. J.; O'Neill, H. S. C.; Jayasuriya, K. D.; Campbell, S. J.; Foran, G. J. XANES Calibrations for the Oxidation State of Iron in a Silicate Glass. *Am. Mineral.* **2003**, *88* (7), 967−977.
(37) Berry, A. J.; Stewart, G. A.; O'Neill, H. S. C.; Mallmann, G.; Mosselmans, J. F. W. A Re-Assessment of the Oxidation State of Iron in MORB Glasses. *Earth Planet. Sci. Lett.* **2018**, *483*, 114−123.
(38) Nomura, R.; Ozawa, H.; Tateno, S.; Hirose, K.; Hernlund, J.; Muto, S.; Ishii, H.; Hiraoka, N. Spin Crossover and Iron-Rich Silicate Melt in the Earth's Deep Mantle. *Nature* **2011**, *473* (7346), 199−202.
(39) Gu, C.; Catalli, K.; Grocholski, B.; Gao, L.; Alp, E.; Chow, P.; Xiao, Y.; Cynn, H.; Evans, W. J.; Shim, S.-H. Electronic Structure of Iron in Magnesium Silicate Glasses at High Pressure. *Geophys. Res. Lett.* **2012**, *39* (24), L24304.
(40) Mao, Z.; Lin, J.-F.; Yang, J.; Wu, J.; Watson, H. C.; Xiao, Y.; Chow, P.; Zhao, J. Spin and Valence States of Iron in Al-Bearing Silicate Glass at High Pressures Studied by Synchrotron Mössbauer and X-Ray Emission Spectroscopy. *Am. Mineral.* **2014**, *99* (2−3), 415−423.
(41) De Groot, F.; Kotani, A. *Core Level Spectroscopy of Solids*; CRC Press, 2008.
(42) Glatzel, P.; Bergmann, U. High Resolution 1s Core Hole X-Ray Spectroscopy in 3d Transition Metal Complexes - Electronic and Structural Information. *Coord. Chem. Rev.* **2005**, *249* (1−2), 65−95.
(43) Lin, J.-F.; Mao, Z.; Jarrige, I.; Xiao, Y.; Chow, P.; Okuchi, T.; Hiraoka, N.; Jacobsen, S. D. Resonant X-Ray Emission Study of the Lower-Mantle Ferropericlase at High Pressures. *Am. Mineral.* **2010**, *95* (8−9), 1125−1131.
(44) Caliebe, W. A.; Kao, C. C.; Hastings, J. B.; Taguchi, M.; Kotani, A.; Uozumi, T.; de Groot, F. M. F. 1*s*2*p* Resonant Inelastic X-Ray Scattering in α-Fe_2O_3. *Phys. Rev. B* **1998**, *58* (20), 13452−13458.
(45) Hayashi, H.; Udagawa, Y.; Caliebe, W. A.; Kao, C. C. Hidden Electronic State of CuO Revealed by Resonant Inelastic X-Ray Scattering. *Phys. Rev. B* **2002**, *66* (3), 033105.
(46) Glatzel, P.; Bergmann, U.; Yano, J.; Visser, H.; Robblee, J. H.; Gu, W.; de Groot, F. M. F.; Christou, G.; Pecoraro, V. L.; Cramer, S. P.; et al. The Electronic Structure of Mn in Oxides, Coordination Complexes, and the Oxygen-Evolving Complex of Photosystem II Studied by Resonant Inelastic X-Ray Scattering. *J. Am. Chem. Soc.* **2004**, *126* (32), 9946−9959.
(47) de Groot, F. M. F.; Glatzel, P.; Bergmann, U.; van Aken, P. A.; Barrea, R. A.; Klemme, S.; Hävecker, M.; Knop-Gericke, A.; Heijboer, W. M.; Weckhuysen, B. M. 1s2p Resonant Inelastic X-Ray Scattering of Iron Oxides. *J. Phys. Chem. B* **2005**, *109* (44), 20751−20762.
(48) Glatzel, P.; Sikora, M.; Fernandez-Garcia, M. Resonant X-Ray Spectroscopy to Study K Absorption Pre-Edges in 3d Transition Metal Compounds. *Eur. Phys. J.* **2009**, *169*, 207−214.
(49) Lundberg, M.; Kroll, T.; DeBeer, S.; Bergmann, U.; Wilson, S. A.; Glatzel, P.; Nordlund, D.; Hedman, B.; Hodgson, K. O.; Solomon, E. I. Metal-Ligand Covalency of Iron Complexes from High-Resolution Resonant Inelastic X-Ray Scattering. *J. Am. Chem. Soc.* **2013**, *135* (45), 17121−17134.
(50) Thomas, R.; Kas, J.; Glatzel, P.; Al Samarai, M.; de Groot, F. M. F.; Alonso Mori, R.; Kavčič, M.; Zitnik, M.; Bucar, K.; Rehr, J. J.; et al. Resonant Inelastic X-Ray Scattering of Molybdenum Oxides and Sulfides. *J. Phys. Chem. C* **2015**, *119* (5), 2419−2426.
(51) Al Samarai, M.; Delgado-Jaime, M. U.; Ishii, H.; Hiraoka, N.; Tsuei, K.-D.; Rueff, J. P.; Lassale-Kaiser, B.; Weckhuysen, B. M.; de Groot, F. M. F. 1s3p Resonant Inelastic X-Ray Scattering of Cobalt Oxides and Sulfides. *J. Phys. Chem. C* **2016**, *120* (42), 24063−24069.
(52) Baker, M. L.; Mara, M. W.; Yan, J. J.; Hodgson, K. O.; Hedman, B.; Solomon, E. I. K- and L-Edge X-Ray Absorption Spectroscopy (XAS) and Resonant Inelastic X-Ray Scattering (RIXS) Determination of Differential Orbital Covalency (DOC) of Transition Metal Sites. *Coord. Chem. Rev.* **2017**, *345*, 182−208.
(53) Kwon, G.; Jang, H.; Lee, J.-S.; Mane, A.; Mandia, D. J.; Soltau, S. R.; Utschig, L. M.; Martinson, A. B. F.; Tiede, D. M.; Kim, H.; et al. Resolution of Electronic and Structural Factors Underlying Oxygen-Evolving Performance in Amorphous Cobalt Oxide Catalysts. *J. Am. Chem. Soc.* **2018**, *140* (34), 10710−10720.
(54) Yan, J. J.; Kroll, T.; Baker, M. L.; Wilson, S. A.; Decréau, R.; Lundberg, M.; Sokaras, D.; Glatzel, P.; Hedman, B.; Hodgson, K. O.; et al. Resonant Inelastic X-Ray Scattering Determination of the

Electronic Structure of Oxyhemoglobin and Its Model Complex. *Proc. Natl. Acad. Sci. U.S.A.* **2019**, *116* (8), 2854−2859.
(55) Cutsail, G. E., III; DeBeer, S. Challenges and Opportunities for Applications of Advanced X-Ray Spectroscopy in Catalysis Research. *ACS Catal.* **2022**, *12* (10), 5864−5886.
(56) Wang, J.; Hsu, C.-S.; Wu, T.-S.; Chan, T.-S.; Suen, N.-T.; Lee, J.-F.; Chen, H. M. In Situ X-Ray Spectroscopies Beyond Conventional X-Ray Absorption Spectroscopy on Deciphering Dynamic Configuration of Electrocatalysts. *Nat. Commun.* **2023**, *14* (1), 6576.
(57) Rueff, J. P.; Journel, L.; Petit, P. E.; Farges, F. Fe *K* Pre-Edges as Revealed by Resonant X-Ray Emission. *Phys. Rev. B* **2004**, *69* (23), 235107.
(58) Kim, J.; Shvyd'ko, Y.; Ovchinnikov, S. G. Charge Transfer and Mott-Hubbard Excitations in $FeBO_3$: An Fe *K*-Edge Resonant Inelastic X-Ray Scattering Study. *Phys. Rev. B* **2011**, *83* (23), 235109.
(59) Shvyd'ko, Y. V.; Hill, J. P.; Burns, C. A.; Coburn, D. S.; Brajuskovic, B.; Casa, D.; Goetze, K.; Gog, T.; Khachatryan, R.; Kim, J. H.; et al. MERIX—Next Generation Medium Energy Resolution Inelastic X-Ray Scattering Instrument at the APS. *J. Electron Spectrosc. Relat. Phenom.* **2013**, *188*, 140−149.
(60) Ament, L. J. P.; van Veenendaal, M.; Devereaux, T. P.; Hill, J. P.; van den Brink, J. Resonant Inelastic X-Ray Scattering Studies of Elementary Excitations. *Rev. Mod. Phys.* **2011**, *83* (2), 705−767.
(61) Castillo, R. G.; Hahn, A. W.; Van Kuiken, B. E.; Henthorn, J. T.; McGale, J.; DeBeer, S. Probing Physical Oxidation State by Resonant X-Ray Emission Spectroscopy: Applications to Iron Model Complexes and Nitrogenase. *Angew. Chem.* **2021**, *133* (18), 10200−10209.
(62) Westre, T. E.; Kennepohl, P.; DeWitt, J. G.; Hedman, B.; Hodgson, K. O.; Solomon, E. I. A Multiplet Analysis of Fe *K*-Edge 1*s* → 3*d* Pre-Edge Features of Iron Complexes. *J. Am. Chem. Soc.* **1997**, *119* (27), 6297−6314.
(63) Galoisy, L.; Calas, G.; Arrio, M. A. High-Resolution XANES Spectra of Iron in Minerals and Glasses: Structural Information from the Pre-Edge Region. *Chem. Geol.* **2001**, *174* (1), 307−319.
(64) Glatzel, P.; Mirone, A.; Eeckhout, S. G.; Sikora, M.; Giuli, G. Orbital Hybridization and Spin Polarization in the Resonant *1s* Photoexcitations of α-Fe_2O_3. *Phys. Rev. B* **2008**, *77* (11), 115133.
(65) Calas, G.; Petiau, J. Coordination of Iron in Oxide Glasses through High-Resolution *K*-Edge Spectra: Information from the Pre-Edge. *Solid State Commun.* **1983**, *48* (7), 625−629.
(66) Waychunas, G. A.; Apted, M. J.; Brown, G. E. X-Ray K-Edge Absorption Spectra of Fe Minerals and Model Compounds: Near-Edge Structure. *Phys. Chem. Miner.* **1983**, *10* (1), 1−9.
(67) Atkins, A. J.; Bauer, M.; Jacob, C. R. High-Resolution X-Ray Absorption Spectroscopy of Iron Carbonyl Complexes. *Phys. Chem. Chem. Phys.* **2015**, *17* (21), 13937−13948.
(68) Sacconi, L. Five Coordination in 3*d* Metal Complexes. *Pure Appl. Chem.* **1968**, *17* (1), 95−128.
(69) Malki, M.; Magnien, V.; Pinet, O.; Richet, P. Electrical Conductivity of Iron-Bearing Silicate Glasses and Melts. Implications for the Mechanisms of Iron Redox Reactions. *Geochim. Cosmochim. Acta* **2015**, *165*, 137−147.
(70) Kurian, R.; van Schooneveld, M. M.; Zoltan, N.; Vanko, G.; de Groot, F. M. F. Temperature-Dependent 1s2p Resonant Inelastic X-Ray Scattering of CoO. *J. Phys. Chem. C* **2013**, *117* (6), 2976−2981.
(71) Ding, Y.; Fernandez-Rodriguez, J.; Kim, J.; Li, F.; Casa, D.; Upton, M.; Gog, T.; Mao, H.-k.; van Veenendaal, M. Spin-Ordering Mediated Orbital Hybridization in CoO at High Pressures. *Phys. Rev. B* **2012**, *86* (9), 094107.

https://doi.org/10.1021/acs.jpclett.4c03568
J. Phys. Chem. Lett. 2025, 16, 2627−2635